New non-oscillatory central schemes on unstructured triangulations for hyperbolic systems of conservation laws

Ivan Christov [1], Bojan Popov [*]

Department of Mathematics, Texas A&M University, College Station, TX 77843-3368, USA

Abstract

We discuss an extension of the Jiang–Tadmor and Kurganov–Tadmor fully-discrete non-oscillatory central schemes for hyperbolic systems of conservation laws to unstructured triangular meshes. In doing so, we propose a new, "genuinely multidimensional," non-oscillatory reconstruction—the minimum-angle plane reconstruction (MAPR). The MAPR is based on the selection of an interpolation stencil yielding a linear reconstruction with minimal angle with respect to the horizontal. This means that the MAPR does not bias the solution by using a coordinate direction-by-direction approach to the reconstruction, which is highly desirable when unstructured meshes consisting of elements with (almost) arbitrary geometry are used. To show the "black-box solver" capabilities of the proposed schemes, numerical results are presented for a number of hyperbolic systems of conservation laws (in two spatial dimensions) with convex and non-convex flux functions. In particular, it is shown that, even though the MAPR is neither designed with the goal of obtaining a scheme that satisfies a maximum principle in mind nor is total-variation diminishing (TVD), it provides a robust non-oscillatory reconstruction that captures composite waves accurately.
© 2008 Elsevier Inc. All rights reserved.

1. Introduction

Non-oscillatory central schemes are a class of Godunov-type (i.e., shock-capturing, finite volume) numerical methods for solving hyperbolic systems of conservation laws (e.g., the Euler equations of gas dynamics).

[*] Corresponding author. Tel.: +1 979 845 1989; fax: +1 979 862 4190.
  E-mail addresses: christov@northwestern.edu (I. Christov), popov@math.tamu.edu (B. Popov).
  URLs: http://www.esam.northwestern.edu/christov/ (I. Christov), http://www.math.tamu.edu/~popov/ (B. Popov).
 [1] Present address: Department of Engineering Sciences and Applied Mathematics, Northwestern University, Evanston, IL 60208-3125, USA.

Throughout the last decade, central (Godunov-type) schemes have gained popularity due to their simplicity and efficiency. In particular, the latter do not require the solution of a Riemann problem or a characteristic decomposition to compute the intercell flux.

The first second-order accurate non-oscillatory central Godunov-type scheme was introduced by Nessyahu and Tadmor (NT) [1], whose work generalized the first-order accurate *staggered* Lax–Friedrichs scheme using a non-oscillatory piecewise-linear reconstruction in the spirit of van Leer's MUSCL [2]. The NT scheme, which is one of the simplest and most versatile Godunov-type numerical methods, has recently been put on solid theoretical ground by the proof of the fully-nonlinear scheme's convergence to the unique entropy solution of the problem in the case of strictly convex nonlinear scalar conservation laws [3]. In addition, over the last decade, the NT scheme has inspired a significant amount of research on the topic of non-oscillatory central schemes. Some of the recent work on central schemes includes, but is not limited to, semi-discrete formulations, less dissipative central-upwind schemes, extensions to multiple spatial dimensions and non-Cartesian meshes (see, e.g., [4–13] and the references therein).

In this paper, we present an extension of the second-order accurate (in space and time) two-dimensional (2D) central scheme of Jiang and Tadmor (JT) [5,13], which is the 2D version of the Nessyahu–Tadmor scheme, to unstructured triangulations. To be precise, however, we propose a Jiang–Tadmor-*like* scheme because the staggered control volumes are "fixed," i.e., they are determined entirely from the non-staggered ones. However, unlike the schemes in [1,5], in the extensions proposed herein we complete each time step with a reconstruction on the staggered mesh followed by a projection onto the original triangulation. The latter idea was first introduced by Jiang et al. [6] to "unstagger" the NT and JT schemes. The main advantage of this approach is that it makes the implementation of boundary conditions considerably simpler, and it does not require the *staggered* staggered mesh to coincide with the original one—a fact that is always true for Cartesian tensor-product grids but generally not true for unstructured meshes. With hindsight, we formulated the scheme in this manner to allow for the seamless incorporation of recent developments in central schemes, which we shall now discuss.

The JT scheme has been further refined by Kurganov and Tadmor (KT) [7] (the so-called *modified central differencing scheme*) by making use of the maximal local speeds of propagation in constructing the staggered mesh's cells. In doing so, the scheme's numerical diffusion becomes independent of the inverse of the time step size, which allows (in particular) a semi-discrete formulation of the method. In this paper, we also present an extension of the KT scheme to unstructured triangulations, which might be preferable (over the JT-type scheme) for certain problems due to its reduced numerical diffusion.

In light of the work of Kurganov and Petrova [11], which extended the "state-of-the-art" semi-discrete central-upwind schemes [8] to triangular meshes, we must provide further motivation for the present work. Our goal is to build a very simple *fully*-discrete central scheme on (truly) unstructured triangulations. This is unlike the central-upwind scheme in [11] because, even though the semi-discrete limit results in a "nice" closed-form expression for the system of ordinary differential equations (ODEs) governing the evolution of the cell averages, on a truly unstructured mesh the system of ODEs is different for each cell due to the latter's dependance on local mesh-connectivity information. This presents serious problems for the implementation of adaptive mesh refinement. Moreover, for purely hyperbolic equations, it was reported in [7, p. 270] that the fully discrete central scheme's performance is comparable to that of the semi-discrete one when the staggered mesh is built via the modified-central-differencing approach, which we show how to do for a triangulation.

Furthermore, in the context of the JT- and KT-type fully-discrete central schemes we discuss in this paper, we propose a novel "genuinely-multidimensional" reconstruction, which has the significant advantage (over those available in the literature) of being simple to formulate and implement. Therefore, our work differs fundamentally from that of Arminjon et al. [4], who proposed an extension of the Nessyahu–Tadmor scheme to 2D unstructured triangulations, because of our novel (and simpler) non-oscillatory reconstruction and staggered meshes that fit naturally into the hierarchy of central schemes [7,8,11]. In addition, an important point of the present work, supporting those in the literature, is that unstructured, adaptively-refined meshes can significantly improve the performance of a Godunov-type scheme by keeping discontinuities sharp with a minimal number of mesh elements.

An important goal of this paper, which will be accomplished in future work, is to set the floor for predictor–corrector-type algorithms that couple the (explicit, central) Godunov approach to conservation laws with the

novel (implicit) L^1-minimization finite element method of Guermond and Popov [14,15]. In this vein, we also hope to show how many of the common tools (e.g., tessellation of arbitrary domains, error indicators and adaptive mesh refinement, etc.) of finite-element methods can be seamlessly incorporated into Godunov-type finite-volume schemes. This interconnection between the "classical" finite element building blocks and Godunov-type schemes would allow for the construction of algorithms and software for the computation of complex physical flows where, e.g., one must solve coupled systems of hyperbolic and elliptic equations. Such systems commonly arise in the modeling of fluid flow in oil reservoirs (see, e.g., the review article of Gerritsen and Durlofsky [16]), where computing the (nonlinear) advective contributions in the model proves to be most challenging. In this respect, as the recent work of Käser and Iske [17] shows, Godunov-type schemes (in conjunction with unstructured, adaptively refined meshes) have proven to be an effective tool for petroleum reservoir flow simulations.

Finally, this paper is organized as follows. In Section 1.1, the problem is stated and basic notation for the paper is set out. In Section 2, the numerical method is described, including the reconstruction, evolution and projection steps. Finally, in Section 3, several numerical examples, including scalar equations (with both convex and non-convex fluxes), two-phase reservoir flow and the Euler system of gas dynamics, are presented and discussed.

1.1. Statement of the problem and notation

We consider the following initial-value problem for a 2D *hyperbolic* system of conservation laws:

$$\begin{cases} \partial_t \boldsymbol{q} + \partial_x \boldsymbol{f}(\boldsymbol{q}) + \partial_y \boldsymbol{g}(\boldsymbol{q}) = \boldsymbol{0}, & (x, y, t) \in \Omega \times (0, T], \\ \boldsymbol{q}(x, y, t = 0) = \boldsymbol{q}_0(x, y), & (x, y) \in \Omega, \end{cases} \tag{1}$$

where $\Omega \subset \mathbb{R}^2$ is the interior of a polygonal domain, whose boundary we denote by $\partial\Omega$. In addition, let $\mathcal{T}$ be a *conforming* triangulation (see, e.g., [18, p. 56]) of $\overline{\Omega} := \Omega \cup \partial\Omega$, i.e., a finite collection of, say, N subsets τ of $\overline{\Omega}$, called elements, each of which is a non-degenerate triangle (usually satisfying a minimum-angle condition). We denote by $|\tau|$ the area of an element $\tau \in \mathcal{T}$.

Furthermore, w stands for the approximation to $\boldsymbol{q}$, the true solution to (1), on the triangulation $\mathcal{T}$. Then, the constant $\bar{w}_i^n$ represents the approximate average of the solution over the element $\tau_i \in \mathcal{T}$ at time $t = t^n$, i.e.,

$$\bar{\boldsymbol{w}}_i^n \approx \bar{\boldsymbol{q}}_i^n := \frac{1}{|\tau_i|} \int\int_{\tau_i} \boldsymbol{q}(x, y, t^n) \mathrm{d}A, \tag{2}$$

where $\mathrm{d}A := \mathrm{d}x\mathrm{d}y$. Moreover, given a fixed time step Δt, we define $t^n := n\Delta t$.

Finally, throughout the text we represent points in Euclidean space by ordered pairs, e.g. (x, y). However, if an ordered pair is followed by a $\top$ superscript, e.g. $(v_x, v_y)^\top$, it stands for a (column) vector. In addition, a dot between two vectors denotes the usual Euclidean inner product.

2. Overview of the scheme

2.1. Reconstruction

Without loss of generality, we restrict ourselves to the case of a scalar conservation law for the rest of this section. In the case of a system, the procedure described herein is applied to each component of w (i.e., each equation) in the same manner.

Thus, to approximate (1), we begin each time step with a piecewise-constant solution of the form

$$\bar{w}^n(x, y) = \sum_{i=1}^{N} \bar{w}_i^n \chi_i(x, y), \tag{3}$$

where χ_i is the characteristic function of the element τ_i, i.e.,

$$\chi_i(x, y) = \begin{cases} 1, & \text{if } (x, y) \in \tau_i; \\ 0, & \text{otherwise.} \end{cases} \tag{4}$$

Then, we construct a piecewise-polynomial interpolant of $\bar{w}^n$:

$$w^n(x,y) = \sum_{i=1}^{N} p_i^n(x,y)\chi_i(x,y), \tag{5}$$

where, for the purposes of this paper, p_i^n is a linear function in two variables. We require the reconstruction to be conservative, hence we must have that at the center of mass of the element τ_i, which we denote by (x_i^*, y_i^*), $w^n(x_i^*, y_i^*) \equiv p_i^n(x_i^*, y_i^*) = \bar{w}_i^n$. Consequently, the linear interpolant has the following explicit form:

$$p_i^n(x,y) = \bar{w}_i^n + \nabla p_i^n \cdot (x - x_i^*, y - y_i^*)^\top. \tag{6}$$

Clearly, the gradient ∇p_i^n uniquely determines each linear interpolant.

There has been a significant amount of work on how to choose ∇p_i^n on an unstructured triangulation so that the piecewise-linear reconstruction (5) is non-oscillatory: slope-limited nearest-neighbor linear interpolation [19] and its maximum-principle-satisfying versions [20,21], slope-limited least-squares gradient recovery [4], "admissible" piecewise-linear reconstruction [22,11], essentially non-oscillatory (ENO) reconstruction [23], weighted ENO (WENO) reconstruction [24,25], limiter-free hyperbolic and logarithmic reconstructions [26,27], etc. It should be noted here that there is another class of reconstruction/limiting procedures on unstructured triangulations, with desirable and provable theoretical (e.g., stability, positivity) properties, that have been developed in the works of [28,29], but the latter require a local characteristic decomposition, so they cannot be directly applied (componentwise) to the conserved variables as the former methods. Finally, we refer the reader to [30, pp. 212–225] and [31, pp. 31–41] for a more comprehensive overview of non-oscillatory reconstruction on unstructured meshes.

Though there has been a significant amount of progress on this subject, many of the above-mentioned methods feature empirical parameters and ad-hoc assumptions, which we do not find robust. To this end, we propose the *minimum-angle plane reconstruction*, which is closest to the approaches in [19–21], but also adds a bit of an ENO/UNO [32] "flavor" to the reconstruction (i.e., there is no reduction to first order near extrema). In other words, rather than striving to achieve a scheme that is TVD or satisfies a maximum principle, we take a pragmatic approach to the reconstruction, using fully the much larger number of degrees of freedom in 2D.

To this end, consider an element $\tau_i \in \mathcal{T}$ and its first (also known as the *level-0 von Neumann* [17,33]) neighbors, which we define as those elements of $\mathcal{T}$ that share an edge with τ_i. Henceforth, we refer to the first neighbors of an element simply as neighbors, and explicitly state if we are referring to other ones. For a triangulation of the type discussed in Section 1.1, τ_i may have either one, two or three neighbors, which we denote by τ_{i1}, τ_{i2} and τ_{i3} (see Fig. 1). There are two cases that require special attention. First, if τ_i has only
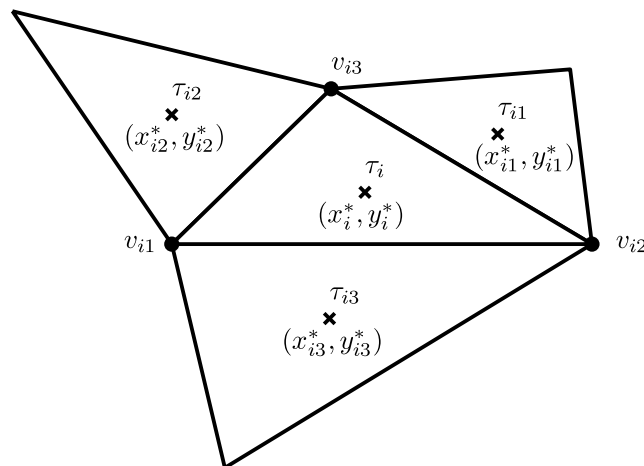

Fig. 1. Diagram of an element of the triangulation and its first neighbors.

two neighbors (i.e., one of τ_i's edges lies on $\partial\Omega$), then only one plane can be constructed and it is the minimum-angle plane. Second, if τ_i has only one neighbor (i.e., two of τ_i's edges lie on $\partial\Omega$) then its second and third neighbors are defined as the two neighbors of τ_i's first neighbor that are not τ_i itself.

Now, for the two cases when three neighbors of $\tau_i \in \mathcal{T}$ can be identified, we begin the minimum-angle plane reconstruction by finding the four planes that pass through the following collections of points (see Fig. 1):

(i) $(x_i^*, y_i^*, \bar{w}_i^n), (x_{i1}^*, y_{i1}^*, \bar{w}_{i1}^n), (x_{i2}^*, y_{i2}^*, \bar{w}_{i2}^n)$;
(ii) $(x_i^*, y_i^*, \bar{w}_i^n), (x_{i2}^*, y_{i2}^*, \bar{w}_{i2}^n), (x_{i3}^*, y_{i3}^*, \bar{w}_{i3}^n)$;
(iii) $(x_i^*, y_i^*, \bar{w}_i^n), (x_{i3}^*, y_{i3}^*, \bar{w}_{i3}^n), (x_{i1}^*, y_{i1}^*, \bar{w}_{i1}^n)$;
(iv) $(x_{i1}^*, y_{i1}^*, \bar{w}_{i1}^n), (x_{i2}^*, y_{i2}^*, \bar{w}_{i2}^n), (x_{i3}^*, y_{i3}^*, \bar{w}_{i3}^n)$.

For a continuous linear function, each of the latter sets of three points defines its gradient exactly. It should be noted here that the identification of the gradient with a plane, in the above manner, was first suggested in [20]. However, we take the analogy a step further. Upon identifying the four (in this case) possible planes, we compute the limited gradient from the plane that concludes the smallest angle with the horizontal. The angle is always corrected to the first quadrant because the orientation of the plane is not significant.

That is to say, let $v \equiv (v_x, v_y, v_z)^\top$ be the *unit* normal vector to any of the above planes. And, if we denote by P_1, P_2 and P_3 the vectors from the origin of $\mathbb{R}^3$ to the three points defining said plane, then we simply have that

$$v = \frac{(P_3 - P_1) \times (P_2 - P_1)}{\|(P_3 - P_1) \times (P_2 - P_1)\|}, \tag{7}$$

where $\times$ denotes the cross (or vector) product and $\|\cdot\|$ the usual Euclidean norm over $\mathbb{R}^3$. Then, the angle of the latter plane with respect to the horizontal is given by

$$\theta = \begin{cases} \arccos(v_z), & \text{if } \arccos(v_z) \leqslant \frac{\pi}{2}; \\ \pi - \arccos(v_z), & \text{otherwise.} \end{cases} \tag{8}$$

Now suppose we have found the minimum-angle plane (by choosing the one for which θ is least) over some $\tau_i \in \mathcal{T}$ at $t = t^n$, and its unit normal is v as above, then it is easy to show that

$$\nabla p_i^n = \begin{cases} -(v_x/v_z, v_y/v_z)^\top, & \text{if } v_z > \epsilon; \\ (0,0)^\top, & \text{otherwise.} \end{cases} \tag{9}$$

The second case in the above conditional is required to prevent the selection of a vertical minimum-angle plane. The tolerance ϵ can be taken to be machine accuracy or something slightly larger (e.g., 10^{-10} as done in [21]) to be safe. Thus, the piecewise-linear reconstruction (5) of the piecewise-constant data (3) is complete.

2.1.1. Modifying the reconstruction for boundary elements

Due to lack of information at the boundaries—boundary elements have only one or two neighbors—we add the boundary elements' *second neighbors* (i.e., their neighbors' neighbors or level-1 von Neumann neighbors [17,33]) to the set of possible points through which the minimum-angle plane may pass. This results in stable interpolation at the boundaries and does not degrade the solution. Though the latter modification of the interpolation stencil is unnecessary for smooth solutions, it is crucial for solutions that feature a discontinuity oblique to the boundary. In fact, the second neighbors may be used in the selection of the minimum-angle plane for interior elements as well, if a more dissipative reconstruction is necessary for a certain problem.

2.2. Evolution

2.2.1. Construction of the staggered mesh

In order to avoid solving Riemann problems at the interfaces of the elements in $\mathcal{T}$, we define a staggered mesh $\mathcal{S}$, whose elements contain the Riemann fans emanating from the discontinuities in the piecewise-linear approximate solution (5). Then, we realize the solution at the next time step by its averages over elements of $\mathcal{S}$. Note that we are no longer restricting the discussion to the scalar case, as in Section 2.1.

To this end, assuming a suitable CFL condition holds, the discontinuities in w^n along the edges and at the vertices of each $\tau_i \in \mathcal{T}$ cannot propagate into the sub-triangle Δ_i, whose vertices are located at *one-third* of the distance from the vertices of τ_i, $\{v_{ij}\}_{j \in \{1,2,3\}}$ (recall Fig. 1), to its center of mass (x_i^*, y_i^*). Since the discontinuities in w^n at every vertex can propagate into all elements of $\mathcal{T}$ that share it, we define Λ_{ij} to be the polygonal domains about each vertex of τ_i, in which the piecewise-linear interpolant (5) is discontinuous due to the jumps emanating from those edges (of τ_i and its neighbors) that share the vertex; here, $j \in \{1, 2, 3\}$ is an index over the vertices of τ_i. Furthermore, we define Π_{ij} to be the parallelograms that contain the discontinuities emanating from the edges of τ_i only; now, $j \in \{1, 2, 3\}$ is an index over the neighbors of τ_i. Fig. 2 illustrates the elements of the staggered mesh $\mathcal{S} = \cup_{i,j}\{\Delta_i, \Lambda_{ij}, \Pi_{ij}\}$ that overlap with some $\tau_i \in \mathcal{T}$.

Of course, the construction described above is by no means unique. For example:

(i) If $|\Delta_i| = |\Pi_{ij}| \equiv 0 \ \forall i, j$, then the staggered mesh becomes the well-known Voronoi diagram, which is commonly used in finite-volume discretizations of elliptic problems (see [18, pp. 262–265] and [31, pp. 44–45]).
(ii) If the maximal local speeds of propagation (at the vertices of τ_i) are used to determine the location of the vertices of Δ_i, while keeping them on the line segment connecting the original vertex of τ_i to its center of mass, we get an analogue of Kurganov and Tadmor's (KT) modified central differencing [7] for unstructured triangulations.

Also, there is nothing special about the factor of $\frac{1}{3}$ used in the construction, we chose it because it results in a fixed (thus Jiang–Tadmor-type) staggered mesh, which is not the Voronoi diagram, and therefore the scheme is *less diffusive* than the immediate extension of the JT scheme to triangulations. In this respect, our (unstructured) staggered mesh is quite distinct from the ones proposed by Arminjon et al. [4,9] because it introduces *three* types of staggered elements, meanwhile the latter authors employ a single type. Breaking down the staggered mesh into these building blocks not only makes our scheme less diffusive than the ones of JT-type (such as those of Arminjon et al.), but also simplifies the discussion and construction of a KT-type staggered mesh. Furthermore, it is important to realize that these are the same three *types* of staggered elements that Kurganov and Petrova [11] use to derive their central-upwind scheme on triangulations.

To this end, we must explain what we mean by maximal local speed of propagation, which we denote by $a_j^{\max}(\tau_i)$, where $j \in \{1, 2, 3\}$ counts the vertices of τ_i. This is the maximum speed at which a discontinuity at the jth vertex of $\tau_i \in \mathcal{T}$ may propagate into the sub-triangle $\Delta_i \subset \tau_i$ (see also [11]). Therefore, we may take

$$a_j^{\max}(\tau_i) = \max\{\max_{\boldsymbol{\xi} \in \mathcal{C}(v_{ij})} \rho[J(\boldsymbol{\xi})], \kappa\}, \tag{10}$$
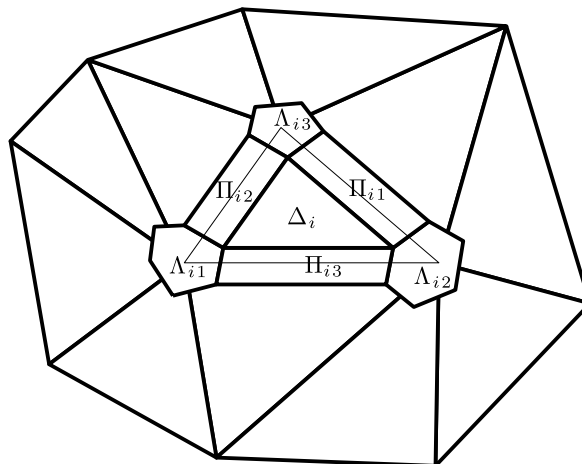

Fig. 2. Diagram of the JT-type staggered mesh superimposed onto the triangulation.

$\mathcal{C}(v_{ij})$ is the curve in phase space that connects the states $\{\boldsymbol{p}_k^n(v_{ij})\}_{k \in \mathcal{N}(v_{ij})}$ with $\mathcal{N}(v_{ij})$ being the set of indices of the elements that share the vertex v_{ij}, and $\rho(A)$ denotes the spectral radius of a matrix A (i.e., $\max_l |\lambda_l(A)|$, where $\lambda_l(A)$ is an eigenvalue of A). Moreover, J is the Jacobian matrix defined as

$$J(\boldsymbol{\xi}) := v_x \frac{\partial \boldsymbol{f}}{\partial \boldsymbol{q}}(\boldsymbol{\xi}) + v_y \frac{\partial \boldsymbol{g}}{\partial \boldsymbol{q}}(\boldsymbol{\xi}), \tag{11}$$

where [in the context of (10)] v_x and v_y are the components of the unit vector along the line segment from the jth vertex of τ_i to its center of mass, and $\boldsymbol{\xi}$ is a vector of conserved quantities.

Some remarks about the KT-type staggered mesh are in order here:

(i) We require that $a_j^{\max}(\tau_i) \neq 0 \ \forall i, j$ via the tolerance κ, which we take to be 10^{-6}, because if that were to happen then there would be degenerate staggered elements (i.e., ones with zero area) in the staggered mesh $\mathcal{S}$, which would make the reconstruction on $\mathcal{S}$ much more complicated. Thus, since the goal of Kurganov and Tadmor's modified central differencing [7] is to make the staggered elements' area of order $\mathcal{O}(\Delta t)$ (actually, $\mathcal{O}[(\Delta t)^2]$ in the case of the polygonal staggered elements), we may replace the degenerate staggered elements with "very small" ones without affecting the performance of the KT-type scheme.

(ii) For the case of a convex flux, (10) simply reduces to

$$a_j^{\max}(\tau_i) = \max\{\max_{k \in \mathcal{N}(v_{ij})} \rho(J[\boldsymbol{p}_k^n(v_{ij})]), \kappa\}. \tag{12}$$

(iii) The observant reader might notice that this definition of the KT-type staggered mesh differs from the one that comes from simplifying the central-upwind staggered mesh of Kurganov and Petrova [11]. This is because we want to keep each inner triangle Δ_i similar to its "parent" triangle τ_i, in order to maintain the quality of the staggered mesh. That is, we do not allow the staggered mesh to become very deformed in parts of the domain (e.g., elements with small area neighboring elements with large area), but we *do* use the local speeds of propagation to reduce the numerical diffusion of the scheme à la the modified central differencing. In this vein, we also make sure that none of the elements of the KT-type staggered mesh exceed the size of the corresponding ones of the JT-type mesh.

Now, since we require that $|\Delta_i| \neq 0 \ \forall i$ and that the vertices of Δ_i fall in a smooth region of the flow, we readily obtain a geometric CFL-like condition on the time-step size. Though this condition is not based on a stability analysis of the scheme, it results in a non-oscillatory and stable method, as shown by the numerical results in Section 3. For the JT-type staggered mesh we assumed, above, that the sub-triangles' vertices are always located at one-third of the distance from the original triangle's vertices to its center of mass. Hence, by considering the maximal wave speed and the "smallest" triangle in the mesh, we find that we must require that

$$a^{\max} \Delta t \leqslant \frac{1}{9} \min_{\tau_i \in \mathcal{T}} \min_{1 \leqslant j \leqslant 3} h_j(\tau_i), \tag{13}$$

where $h_j(\tau_i)$ is the altitude of τ_i onto its jth side, and

$$a^{\max} := \max_{\tau_i \in \mathcal{T}} \max_{1 \leqslant j \leqslant 3} a_j^{\max}(\tau_i) \tag{14}$$

is the maximal wave speed over the whole mesh (or a proper upper bound of it). Thus, the "effective" CFL number is $C_{\mathrm{CFL}} = \frac{1}{9}$. For the KT-type staggered mesh, the condition is less restrictive, since (in some sense) we optimize the sizes of the staggered mesh elements:

$$a^{\max} \Delta t \leqslant \frac{1}{3} \min_{\tau_i \in \mathcal{T}} \min_{1 \leqslant j \leqslant 3} h_j(\tau_i). \tag{15}$$

This gives an effective CFL number of $C_{\mathrm{CFL}} = \frac{1}{3}$. The latter CFL condition is the equivalent to the one used in [11], and similar to the one in [19,27,17,33]. Furthermore, both of the above CFL-like conditions are far less restrictive than the ones used for the upwind schemes presented in [21,22] and the 3D central scheme featured

in [10], where the right-hand side of the equivalent of (15) has term proportional to the minimal triangle altitude *squared*. Furthermore, our numerical results suggest that the JT-type scheme is actually stable under the less-restrictive CFL condition (15), so we use a CFL number of $\frac{1}{3}$ in practice, instead of the theoretical maximum of $\frac{1}{9}$, when possible. This is not surprising, since (13) is a sufficient but not necessary condition due to the right-hand side being an estimate from above.

To summarize, the vertices of $\Delta_i \subset \tau_i$, denoted by $\{v_{ij}^*\}_{j\in\{1,2,3\}}$, are given by

$$v_{ij}^* = \frac{2}{3} v_{ij} + \frac{1}{3} g_i \tag{16}$$

for the JT-type staggered mesh, where $g_i \equiv (x_i^*, y_i^*)$ (recall Fig. 1). And, similarly, the vertices of the inner triangle are given by

$$v_{ij}^* = \left(1 - \frac{a_j^{\max}\Delta t}{|\overrightarrow{v_{ij}g_i}|}\right)v_{ij} + \frac{a_j^{\max}\Delta t}{|\overrightarrow{v_{ij}g_i}|} g_i \tag{17}$$

for the KT-type staggered mesh, where $|\overrightarrow{v_{ij}g_i}|$ denotes the length of the line segment connecting v_{ij} to g_i. The latter two equations essentially define the entire staggered mesh $\mathcal{S}$. The only other "ingredient" one needs is the staggered elements' connectivities, which follow directly from the connectivities (vertex to edge, vertex to element and element to edge) of the original triangulation $\mathcal{T}$.

2.2.2. Evolution of the staggered averages

Now, we evolve the piecewise-linear function (5) according to the conservation law (1) over the *staggered* mesh $\mathcal{S}$ rather than the original triangulation $\mathcal{T}$. To this end, we require that the approximate solution w satisfy (1) subject to the initial condition $w(x, y, t^n) = w^n(x, y)$. We proceed by integrating the equation over $\sigma_k \times [t^n, t^{n+1}]$, where $\sigma_k \in \mathcal{S}$ is any one of the staggered elements described above. Then, after applying the fundamental theorem of calculus to the temporal integral of w_t, we obtain

$$\bar{w}_k^{n+1} = \bar{w}_k^n - \frac{1}{|\sigma_k|} \int_{t^n}^{t^{n+1}} \iint_{\sigma_k} \partial_x \boldsymbol{f}(w) + \partial_y \boldsymbol{g}(w) \mathrm{d}A\mathrm{d}t, \tag{18}$$

where $\bar{w}_k^{n+1}$ denotes the (staggered) average of w over σ_k at $t = t^{n+1}$. Moreover, it follows from the initial condition that

$$\bar{w}_k^n = \frac{1}{|\sigma_k|} \iint_{\sigma_k} w^n(x, y) \mathrm{d}A. \tag{19}$$

Note that, since w^n is a *piecewise-linear* function, the integral in (19) can be evaluated *exactly* by the midpoint quadrature rule, provided that it is split up into a sum of integrals over parts of σ_k on which w^n is smooth.

We proceed by applying the divergence theorem to the spatial integral on the right-hand side of (18) to get

$$\bar{w}_k^{n+1} = \bar{w}_k^n - \frac{1}{|\sigma_k|} \int_{t^n}^{t^{n+1}} \oint_{\partial\sigma_k} \boldsymbol{f}(w)v_x + \boldsymbol{g}(w)v_y \mathrm{d}s\mathrm{d}t, \tag{20}$$

where $\partial\sigma_k$ denotes the boundary of σ_k, $\boldsymbol{v} \equiv (v_x, v_y)^\top$ denotes the *unit outward* normal vector to $\partial\sigma_k$ and $(\mathrm{d}s)^2 = (\mathrm{d}x)^2 + (\mathrm{d}y)^2$. Note that everything up to this point is *exact*.

We continue by employing the *midpoint* quadrature rule to approximate the temporal integral on the right-hand side of (20), admitting a $\mathcal{O}[(\Delta t)^2]$ local truncation error. Since we assumed the appropriate CFL condition holds so that the discontinuities in the solution do not leave the staggered mesh's elements during the current time step, the solution at $t = t^{n+\frac{1}{2}}$ is smooth along $\partial\sigma_k$, and so we are justified in using the midpoint rule (in time), and we have formal second-order accuracy in time. Consequently,

$$\bar{w}_k^{n+1} \approx \bar{w}_k^n - \frac{\Delta t}{|\sigma_k|} \oint_{\partial\sigma_k} \boldsymbol{f}(w(x, y, t^{n+\frac{1}{2}}))v_x + \boldsymbol{g}(w(x, y, t^{n+\frac{1}{2}}))v_y \mathrm{d}s, \tag{21}$$

where $t^{n+\frac{1}{2}} := \frac{1}{2}(t^n + t^{n+1}) \equiv (n + \frac{1}{2})\Delta t$. Alternatively, one could use the improved (though still second order) quadrature rule presented in [34] for the temporal integral.

In the spirit of the Jiang–Tadmor predictor–corrector scheme [5], we proceed by predicting the temporal midvalues, i.e., $w(x, y, t^{n+\frac{1}{2}})$, by assuming that the point (x, y) is located away from discontinuities, which is the case at the chosen points of evaluation (see below) along $\partial\sigma_k$. To this end, we expand w in a Taylor series in time about $t = t^n$, neglect all terms of $\mathcal{O}[(\Delta t)^2]$, and use the conservation law (1) to replace $\partial_t w$ by a known quantity (see [5]) to obtain

$$w(x, y, t^{n+\frac{1}{2}}) \approx w^n(x, y) - \frac{\Delta t}{2}\left[\frac{\partial f}{\partial q}(w^n(x, y))\frac{\partial w^n}{\partial x} + \frac{\partial g}{\partial q}(w^n(x, y))\frac{\partial w^n}{\partial y}\right], \tag{22}$$

where $\partial f/\partial q$ and $\partial g/\partial q$ are the Jacobian *matrices* corresponding to the flux functions. In addition, the *vectors* of limited slopes $\partial w^n/\partial x$ and $\partial w^n/\partial y$ above must be conditionally defined so that they take the value of ∇p_i^n over the parts of $\sigma_k \in \mathcal{S}$ that overlap some $\tau_i \in \mathcal{T}$. Finally, we observe that (22) constitutes the predictor step, whereas (21) constitutes the corrector step of the scheme.

We conclude the derivation of the fully-discrete scheme by computing the boundary integral in (21) via the composite *trapezoidal* quadrature rule, since (by construction) $\partial\sigma_k$ consists of a number of line segments whose endpoints are known (see Fig. 2). Consequently, the scheme is, formally, second-order accurate in space and (as already stated) in time.

In order not to belabor the point, we omit the explicit calculation of each line integral in (21), and each double integral in (19), since they depend on the geometry of each of the three different types of elements of $\mathcal{S}$ (see Fig. 2). However, the calculations are straight-forward, though tedious.

2.3. Reconstruction on the staggered mesh

Given an element $\sigma_i \in \mathcal{S}$ and its neighbors $\sigma_{ij}, 1 \leqslant j \leqslant m$, find all $\binom{m+1}{3}$ possible linear functions in two variable that pass through any triplet of points in the collection, each of which is defined as σ_i's (or σ_{ij}'s) center of mass and the value of w^n there. Then, retain the linear reconstruction that concludes the smallest angle with the horizontal, as before, and use it to find a *limited* gradient. Thus, the reconstruction step on the staggered mesh is conceptually (and to a large extent practically) identical to the reconstruction step on the original triangulation.

2.4. Projection/reaveraging onto the triangulation

Finally, we complete each time step by computing the averages over the elements of the original triangulation $\mathcal{T}$ from the piecewise-linear reconstruction of the solution on the staggered mesh $\mathcal{S}$, i.e., $\forall \tau_i \in \mathcal{T}$

$$\bar{w}_i^{n+1} = \frac{1}{|\tau_i|} \int\int_{\tau_i} w^{n+1}(x, y)\mathrm{d}A, \tag{23}$$

which can be evaluated exactly using the (two-dimensional) midpoint quadrature rule, provided it is split-up into integrals over the parts of τ_i on which the integrand is smooth [just like the integral in (19)] because w^{n+1} is a *piecewise*-linear function.

2.5. Implementation of boundary conditions

Following [23,30], we implement boundary conditions by modifying the flux integrals (21) *directly* when $\partial\sigma_k \cap \partial\Omega \neq \emptyset$ (i.e., when we are integrating along the boundary of the domain), rather than modifying the integrals *indirectly* by padding the computational domain with *ghost cells* as commonly done in the literature [35]. Of course, if the mesh is to be truly unstructured, it is not clear whether the concept of a ghost cell (in the usual sense) is well-defined.

3. Numerical results

In this section, we present numerical results for a number of standard test problems and some new ones we propose. With the exception of the results in Section 3.1, we use the JT-type scheme for all calculations due to its simplicity and speed. In particular, since we compute the solution of equations with non-convex fluxes, the evaluation of the maximal local speed of propagation (10) becomes non-trivial (see, e.g., [12]); this complicates the implementation of the KT-type scheme.

3.1. Constant-coefficient linear advection

To show that the schemes presented in Section 2 are indeed second-order accurate in space and time, we solve the following initial-value problem for the "oblique" linear advection equation:

$$\begin{cases} \partial_t u + \partial_x u + \partial_y u = 0, & (x, y, t) \in [0,1]^2 \times (0,1], \\ u(x, y, 0) = \sin[\pi(x+y)], & (x, y) \in [0,1]^2, \end{cases} \tag{24}$$

subject to *exact* boundary conditions on the inflow portions of $\partial\Omega$—i.e., along $x = 0$ and $y = 0$ the values of the conserved quantities are prescribed via the exact solution. It is easy to show that the exact solution to (24) is simply

$$u(x, y, t) = \sin[\pi(x + y - 2t)]. \tag{25}$$

For this problem, we present the accuracy and the estimated (experimental) orders of convergence of the unstructured MAPR-based schemes we proposed above of JT- and KT-type in Tables 1–5, respectively. For the results displayed in Tables 1, 2 and 4, the computations were performed on a structured uniform mesh of Friedrichs–Keller type [18, p.64], pictured in the left panel of Fig. 3, in order to obtain the best possible convergence rates. In order to decrease h (the minimal triangle altitude over the entire mesh) by half from one mesh to the next we perform *uniform refinement* of all elements of the triangulation $\mathcal{T}$. That is to say, each triangle is subdivided into four similar ones by connecting the midpoints of its sides. It is important to note

Table 1
Error in the approximate solution to (24) at $t = 1$ by the JT-type scheme on a *structured uniform* triangulation of Friedrichs–Keller type, as the mesh is refined

# Elements	h	L^∞ error	Order	L^2 error	Order	L^1 error	Order
$8 \times 8 \times 2$	8.839e−2	4.405e−1	–	1.985e−1	–	1.629e−1	–
$16 \times 16 \times 2$	4.419e−2	2.002e−1	1.14	7.481e−2	1.42	5.476e−2	1.57
$32 \times 32 \times 2$	2.210e−2	8.872e−2	1.17	2.818e−2	1.42	1.952e−2	1.49
$64 \times 64 \times 2$	1.105e−2	3.772e−2	1.23	9.254e−3	1.62	5.537e−3	1.82
$128 \times 128 \times 2$	5.524e−3	1.557e−2	1.28	2.951e−3	1.65	1.481e−3	1.90
$256 \times 256 \times 2$	2.762e−3	6.330e−3	1.30	9.372e−4	1.66	3.984e−4	1.89

The CFL number is the maximum possible one, i.e., $C_{\mathrm{CFL}} = \frac{1}{9}$.

Table 2
Error in the approximate solution to (24) at $t = 1$ by the KT-type scheme on a *structured uniform* triangulation of Friedrichs–Keller type, as the mesh is refined

# Elements	h	L^∞ error	Order	L^2 error	Order	L^1 error	Order
$8 \times 8 \times 2$	8.839e−2	2.260e−1	–	8.892e−2	–	6.904e−2	–
$16 \times 16 \times 2$	4.419e−2	9.302e−2	1.28	3.144e−2	1.50	2.178e−2	1.64
$32 \times 32 \times 2$	2.210e−2	3.867e−2	1.27	1.015e−2	1.63	6.341e−3	1.78
$64 \times 64 \times 2$	1.105e−2	1.582e−2	1.29	3.209e−3	1.66	1.788e−3	1.83
$128 \times 128 \times 2$	5.524e−3	6.387e−3	1.31	1.020e−3	1.65	5.102e−4	1.81
$256 \times 256 \times 2$	2.762e−3	2.572e−3	1.31	3.242e−4	1.65	1.449e−4	1.82

The CFL number is the maximum possible one, i.e., $C_{\mathrm{CFL}} = \frac{1}{3}$.

Table 3
Error in the approximate solution to (24) at $t = 1$ by the KT-type scheme on a *unstructured non-uniform* triangulation, as the mesh is refined

# Elements	h	L^∞ error	Order	L^2 error	Order	L^1 error	Order
128	5.573e−2	2.008e−1	–	6.437e−2	–	4.903e−2	–
512	2.787e−2	7.484e−2	1.42	2.291e−2	1.49	1.713e−2	1.52
2048	1.393e−2	3.520e−2	1.09	9.334e−3	1.30	8.010e−3	1.10
8192	6.966e−3	2.063e−2	0.77	2.044e−3	2.19	1.082e−3	2.89
32,768	3.483e−3	1.552e−2	0.41	7.182e−4	1.51	3.239e−4	1.74
131,072	1.742e−3	1.268e−2	0.29	3.074e−4	1.22	1.252e−4	1.37

The CFL number is the maximum possible one, i.e., $C_{\text{CFL}} = \frac{1}{3}$.

Table 4
Error in the approximate solution to (24) at $t = 1$ by the KT-type scheme on a *structured uniform* triangulation of Friedrichs–Keller type, as the mesh is refined

# Elements	h	L^∞ error	Order	L^2 error	Order	L^1 error	Order
$8 \times 8 \times 2$	8.839e−2	2.669e−1	–	1.015e−1	–	7.723e−2	–
$16 \times 16 \times 2$	4.419e−2	1.010e−1	1.40	3.375e−2	1.59	2.301e−2	1.75
$32 \times 32 \times 2$	2.210e−2	4.050e−2	1.32	1.082e−2	1.64	6.734e−3	1.77
$64 \times 64 \times 2$	1.105e−2	1.640e−2	1.30	3.378e−3	1.68	1.876e−3	1.84
$128 \times 128 \times 2$	5.524e−3	6.585e−3	1.32	1.055e−3	1.68	5.131e−4	1.87
$256 \times 256 \times 2$	2.762e−3	2.644e−3	1.32	3.283e−4	1.68	1.363e−4	1.91

The CFL number is the "optimal" one, i.e., $C_{\text{CFL}} = \frac{1}{12}$.

Table 5
Error in the approximate solution to (24) at $t = 1$ by the KT-type scheme on a *unstructured non-uniform* triangulation, as the mesh is refined

# Elements	h	L^∞ error	Order	L^2 error	Order	L^1 error	Order
128	5.573e−2	2.074e−1	–	7.166e−2	–	5.476e−2	–
512	2.787e−2	1.100e−1	0.91	2.368e−2	1.60	1.648e−2	1.73
2048	1.393e−2	3.103e−2	1.83	7.304e−3	1.70	4.507e−3	1.87
8192	6.966e−3	2.286e−2	0.44	2.318e−3	1.66	1.244e−3	1.86
32,768	3.483e−3	1.138e−2	1.01	7.425e−4	1.64	3.600e−4	1.79
131,072	1.742e−3	6.044e−3	0.91	2.505e−4	1.57	1.272e−4	1.50

The CFL number is the "optimal" one, i.e., $C_{\text{CFL}} = \frac{1}{12}$.

that we observe greater than first order of convergence in the L^∞ norm on this type of mesh, unlike the upwind scheme in [19] and its maximum-principle-satisfying versions discussed in [21], while the order of convergence in the L^1 norm is comparable. This supports our claim in Section 2.1 that the MAPR is similar to the Durlofsky–Engquist–Osher [19] limiter but with an ENO/UNO flavor, so that our reconstruction has accuracy greater than first order near extrema.

Furthermore, though the trends are in *excellent* agreement with those reported in [19–22] for fully-discrete *upwind* schemes on triangulations, we do not seem to be able to achieve the full second-order accuracy in the L^∞ norm obtained in [11]. Consequently, we conclude that, even though the MAPR provides a very simple and efficient non-oscillatory reconstruction that results in a (formally) second-order central scheme, the fully-discrete scheme admits more numerical diffusion than the corresponding semi-discrete scheme. The latter erodes the L^∞ order of convergence estimate.

In Tables 3 and 5 we present the (experimental) order of convergence results for the case of the unstructured non-uniform (i.e., $\min_{1 \leqslant j \leqslant 3} h_j(\tau_i)$ varies for different $\tau_i \in \mathcal{T}$) mesh shown in the right panel of Fig. 3. As expected, the numbers do not line up as "nicely" as those for the structured uniform mesh; however, second order of convergence is still observed and, more importantly, the trend in the order of convergence is in agreement with the results reported in [22]. In particular, the results displayed in Table 5 are better than the corresponding ones in [22, Table 2].
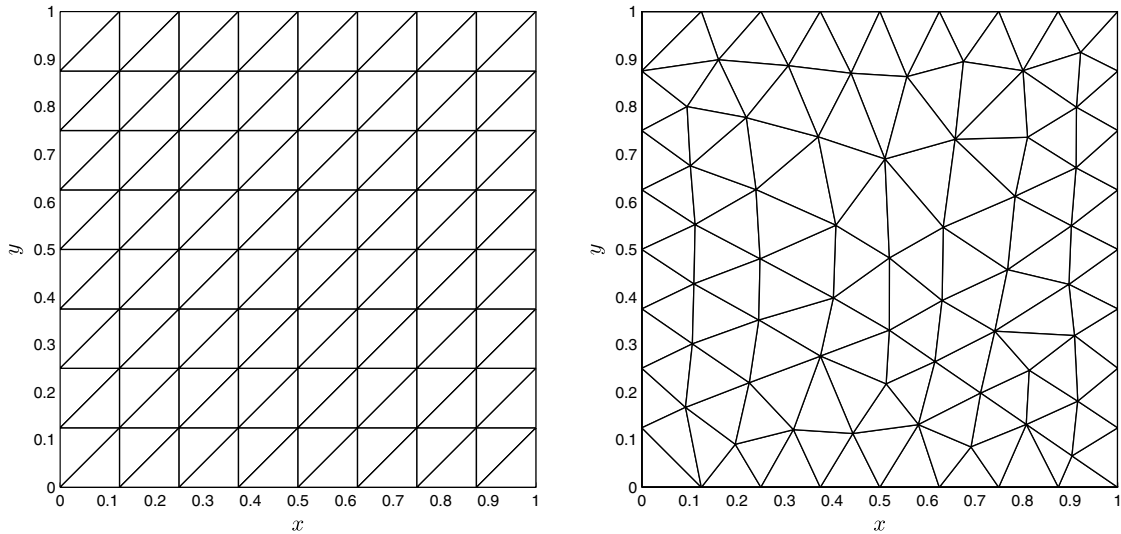
Fig. 3. Coarsest triangulations: structured uniform Friedrichs–Keller (left) and unstructured non-uniform (right).

Finally, we report an interesting phenomenon that we were unable to find in the literature: the existence of an "optimal" CFL number as far as the convergence results of our fully-discrete KT-type central scheme are concerned. That is to say, we found that if the CFL number is taken to be a quarter of the maximum possible one (in our case, this gives $C_{CFL} = \frac{1}{12}$), the (experimental) order of convergence is the best (compare, e.g., Tables 2 and 4), especially in the case of an unstructured mesh (compare Tables 3 and 5). Any larger CFL number gives a worse order of convergence trend, and so does any smaller one (in that case, it is easy to see why—error accumulates from the significantly larger number of time steps). Given the sensitivity of the (experimental) order of convergence on the mesh's structure and the CFL number, and the lack of rigorous convergence estimates for schemes such as this one (in 2D), we must take the results reported above (and the corresponding ones in our references) with a grain of salt.

3.2. Inviscid Burgers equation

Next, we solve the following well-known scalar equation:

$$\partial_t u + \partial_x \left(\frac{1}{2} u^2\right) + \partial_y \left(\frac{1}{2} u^2\right) = 0, \quad (x, y) \in [0, 1]^2, \tag{26}$$

subject to two different initial conditions. First, we consider the "oblique" Riemann problem initial condition

$$u(x, y, 0) = \begin{cases} -1.0, & x > 0.5, \ y > 0.5; \\ -0.2, & x < 0.5, \ y > 0.5; \\ 0.5, & x < 0.5, \ y < 0.5; \\ 0.8, & x > 0.5, \ y < 0.5, \end{cases} \tag{27}$$

in conjunction with *exact* boundary conditions on the inflow portions of $\partial\Omega$. The solution, which is shown in Fig. 4 is advanced to $t = 0.5$, in order for our results to be comparable to those presented in [5]. As can be seen, and it should be no surprise, the resolution of our scheme is comparable to the original JT-type scheme on Cartesian tensor-product grids.

Here, we note that there is no obvious way to select a triangulation that "corresponds" (in some reasonable sense) to a Cartesian tensor-product mesh for the purposes of comparing solutions. For example, in [11] the triangulation was forced to have the same number of elements as the Cartesian mesh, meanwhile in [28] the (minimal) edge length is kept the same. Ultimately, the choice is contingent upon the type of triangulation used. Thus, since we solve the benchmark problems on uniform structured Friedrichs–Keller triangulations
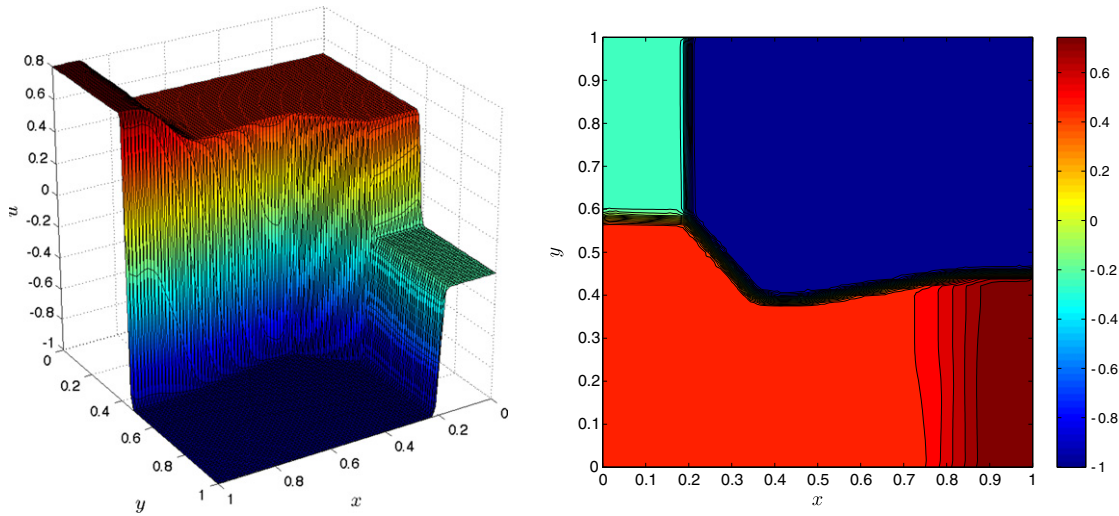
Fig. 4. 3D surface (left) and 2D contour (right) plot of the solution to the Riemann problem (26)–(27) on a Friedrichs–Keller triangulation with 12,800 ($\equiv 80 \times 80 \times 2$) elements; the CFL number is $\frac{1}{3}$.

(recall Fig. 3), which are created by taking a Cartesian tensor-product grid and connecting the "north-east" and "south-west" corners of each square element to form a triangle, we keep the edge length fixed. Thus, all our meshes have exactly twice as many elements as the "corresponding" Cartesian grids.

Next, in order to investigate the order of convergence of our scheme in the presence of genuinely nonlinear waves (i.e., shocks and rarefactions), we consider (26) subject to the following Riemann problem IC:

$$u(x, y, 0) = \begin{cases} 2.0, & x < 0.25, \ y < 0.25; \\ 3.0, & x > 0.25, \ y > 0.25; \\ 1.0, & \text{otherwise}, \end{cases} \qquad (28)$$

in conjunction with exact boundary conditions on the inflow portions of $\partial\Omega$, which (for this problem) are just the parts of Ω along $x = 0$ and $y = 0$. The solution is advanced to $t = \frac{1}{12}$. It consists of two shock waves and two rarefactions that meet towards the middle of the domain to form a cusp. Using the method of characteristics (see, e.g., [35]), the exact solution to this problem, shown in Fig. 5, can be constructed along the diagonals [i.e., lines parallel to $y = x$ along which the 2D problem (26) reduces to a 1D one] and the error in the numerical solution measured. This example is a bit more difficult than the one considered it [22,36] to study the convergence of the scheme to a discontinuous solution; hence, we believe it provides more illuminating (experimental) order of convergence results. The latter are given in Tables 6 and 7. Furthermore, the proper resolution of the cusp that forms in the solution can be used a good benchmark/advertisement for adaptive mesh refinement.

Overall, the convergence results for this problem are in good agreement with those presented in [22,36]. That is to say, the L^1 experimental order of convergence is about one on the structured mesh, and a little worse for the unstructured mesh. This confirms that our scheme is high-order. At the same time, the MAPR prevents any oscillations from arising near the shock waves in the solution.

3.3. A non-convex, nonlinear equation

To demonstrate the robustness of the minimum-angle plane reconstruction, in this section, we consider a benchmark problem proposed in [12], whose solution features a *composite wave*. The equation we wish to solve is the following scalar conservation law with *non-convex* fluxes (i.e., $f''(u)$ and $g''(u)$ change sign):

$$\partial_t u + \partial_x(\sin u) + \partial_y(\cos u) = 0, \quad (x, y, t) \in [-2, 2] \times [-2.5, 1.5] \times (0, 1], \qquad (29)$$
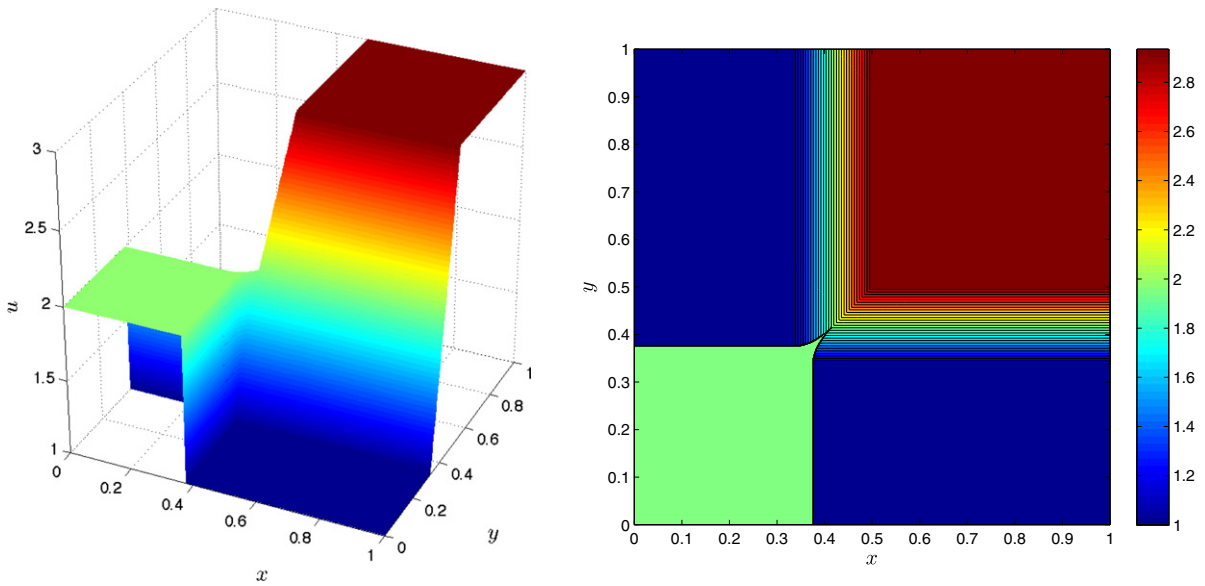
Fig. 5. 3D surface (left) and 2D contour (right) plot of the *exact analytical* solution to the Riemann problem (26)–(28) at $t = \frac{1}{12}$ computed by the method of characteristics.

Table 6
Error in the approximate solution to (26) subject to (28) at $t = \frac{1}{12}$ by the JT-type scheme on a *structured uniform* triangulation of Friedrichs–Keller type, as the mesh is refined

# Elements	h	L^∞ error	Order	L^2 error	Order	L^1 error	Order
$8 \times 8 \times 2$	8.839e−2	7.428e−1	–	2.992e−1	–	2.281e−1	–
$16 \times 16 \times 2$	4.419e−2	6.242e−1	0.25	2.000e−1	0.58	1.371e−1	0.74
$32 \times 32 \times 2$	2.210e−2	6.065e−1	0.04	1.319e−1	0.60	7.772e−2	0.82
$64 \times 64 \times 2$	1.105e−2	5.211e−1	0.22	8.497e−2	0.64	4.130e−2	0.91
$128 \times 128 \times 2$	5.524e−3	5.269e−1	-0.02	5.489e−2	0.63	2.126e−2	0.96
$256 \times 256 \times 2$	2.762e−3	5.098e−1	0.05	3.605e−2	0.61	1.083e−2	0.97

The CFL number is $C_{\mathrm{CFL}} = \frac{1}{9}$.

Table 7
Error in the approximate solution to (26) subject to (28) at $t = \frac{1}{12}$ by the JT-type scheme on a *unstructured non-uniform* triangulation, as the mesh is refined

# Elements	h	L^∞ error	Order	L^2 error	Order	L^1 error	Order
128	5.573e−2	7.155e−1	–	3.574e−1	–	3.001e−1	–
512	2.787e−2	6.916e−1	0.05	2.496e−1	0.52	1.837e−1	0.71
2048	1.393e−2	5.716e−1	0.28	1.699e−1	0.56	1.084e−1	0.76
8192	6.966e−3	5.946e−1	-0.06	1.122e−1	0.60	6.095e−2	0.83
32,768	3.483e−3	6.635e−1	-0.16	7.175e−2	0.65	3.217e−2	0.92
131,072	1.742e−3	6.695e−1	-0.01	4.598e−2	0.64	1.650e−2	0.96

The CFL number is $C_{\mathrm{CFL}} = \frac{1}{9}$.

subject to the Riemman problem initial condition

$$u(x, y, 0) = \begin{cases} 3.5\pi, & x^2 + y^2 < 1; \\ 0.25\pi, & \text{otherwise,} \end{cases} \tag{30}$$

in conjunction with natural (i.e., outflow) boundary conditions on all of $\partial\Omega$. Notice that, for this initial condition, the x-direction flux of (29) has three inflection points, and the y-direction flux has four. This makes the problem more challenging because it gives the limiter/reconstruction more "room for error."

As the results in Fig. 6 show, the MAPR does not suffer from the problems reported in [12] that the less dissipative (more compressive) Superbee limiter and WENO reconstruction do for this non-convex equation. Moreover, the composite wave is captured quite well (especially the curved discontinuity) with a rather small number of elements (compared the 90,000 cells used in [12]) thanks to the *a priori* adaptive refinement of the mesh. This shows the main advantage of using unstructured triangulations instead of Cartesian tensor-product grids: the ability to distribute the computational cells where they are needed.

3.4. Two-phase immiscible incompressible reservoir flow

Next, we consider the flow a two-phase immiscible incompressible fluid. The governing equations for a such a flow (see, e.g., [16,17]) are

$$-\nabla \cdot [\mathbf{K}\lambda_{\text{tot}}(S_{\text{w}})\nabla p] = Q_{\text{tot}}, \tag{31}$$

$$\phi \partial_t S_{\text{w}} + \partial_x[u_{\text{tot}}f(S_{\text{w}})] + \partial_y[v_{\text{tot}}g(S_{\text{w}})] = Q_{\text{w}}, \tag{32}$$

where $\mathbf{K}$ is the absolute permeability tensor, λ_{tot} is the total mobility, p is the thermodynamic pressure, ϕ is the porosity, $S_{\text{w}} \in [0, 1]$ is the water saturation, and $\boldsymbol{u}_{\text{tot}} \equiv (u_{\text{tot}}, v_{\text{tot}})^\top$ is the total velocity (i.e., the sum of the water and oil phase velocities). Eq. (31) is called the *pressure equation*, which is just a statement of Darcy's law combined with the conservation of mass, and (32) is referred to as the *saturation equation*. Once the pressure is computed from (31), the total velocity is given by Darcy's law: $\boldsymbol{u}_{\text{tot}} = \mathbf{K}\lambda_{\text{tot}}(S_{\text{w}})\nabla p$. Finally, in the absence of gravity and capillarity effects the x- and y-direction flux functions $f(\cdot)$ and $g(\cdot)$ are both just the fractional flow function of water, i.e., the non-convex Buckley–Leverett flux:

$$f(S_{\text{w}}) = g(S_{\text{w}}) = \frac{S_{\text{w}}^2}{S_{\text{w}}^2 + \frac{\mu_{\text{w}}}{\mu_{\text{o}}}(1 - S_{\text{w}})^2}, \tag{33}$$

where μ_{w} and μ_{o} are the water and oil phase viscosities, respectively. For simplicity, in the simulations discussed below, we have chosen the following values of the parameters (unless otherwise noted): $\mathbf{K}$ is the 2×2 identity matrix, $\lambda_{\text{tot}}(S_{\text{w}}) \equiv 1$, $\phi \equiv 1$, $Q_{\text{tot}} = Q_{\text{w}} \equiv 0$. Finally, we note that we impose the solid wall (slip) boundary condition $\boldsymbol{u}_{\text{tot}} \cdot \boldsymbol{v} = 0 (\iff \nabla p \cdot \boldsymbol{v} = 0)$ everywhere on the boundary $\partial\Omega$, where $\boldsymbol{v}$ is the outward unit normal to $\partial\Omega$, upon the system (31)–(32). This means that there are no inflow boundaries and, hence, no boundary conditions on S_{w}.
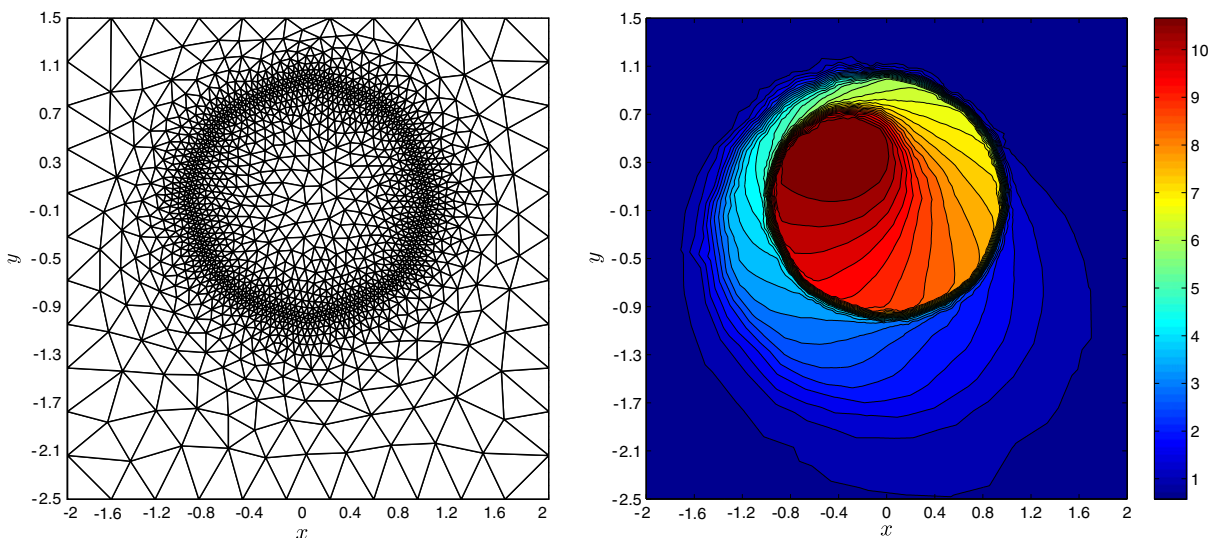

Fig. 6. The *a priori* refined mesh of *only* 3264 elements (left) and a 2D contour (right) plot of the solution to the Riemann problem (29)–(30) at $t = 1.0$; the CFL number is $C_{\text{CFL}} = \frac{1}{3}$.

Note that since Eq. (31) is elliptic it is solved (numerically) using an *implicit* finite element method in practice (see, e.g., [16,19] and the references therein). Then, the complete reservoir flow simulation algorithm [i.e., the solution of (31) by an implicit method, followed by the solution of (32) by an explicit method, such as the one we propose] is called an implicit pressure explicit saturation (IMPES) sequential solver [38]. Therefore, in such a solver, it is crucial to have a fast and extensible scheme for the saturation equation, especially for three-phase and/or multicomponent flows.

3.4.1. Buckley–Leverett equation with gravity

The latter equations are significantly more challenging when gravitational effects are included in the saturation equation, resulting in *different* (non-convex) flux functions in the *x*- and *y*-directions. In this case, $f(\cdot)$ is once again the Buckley–Leverett flux (33), but for the flux in the *y*-direction we have (see, e.g., [37])

$$g(S_{\mathrm{w}}) = f(S_{\mathrm{w}})\Big[1 - C_{\mathrm{g}}(1 - S_{\mathrm{w}})^2\Big], \tag{34}$$

where C_{g} is a constant that depends on the various properties of the medium. Notice that by setting $C_{\mathrm{g}} = 0$ above we recover (33) from (34).

A variation of this problem (one including degenerate diffusion) was solved by the KT central scheme in [7]. Therefore, for comparison purposes, we take $\mu_{\mathrm{w}}/\mu_{\mathrm{o}} = 1.0$ and $C_{\mathrm{g}} = 5.0$ and solve (32) on the square domain $[-1.5, 1.5]^2$ with unit velocity $\boldsymbol{u}_{\mathrm{tot}} \equiv (1,1)^\top$ subject to the (Riemann problem) initial condition:

$$u(x, y, 0) = \begin{cases} 1.0, & x^2 + y^2 < 0.5; \\ 0.0, & \text{otherwise}, \end{cases} \tag{35}$$

which gives rise to a composite-wave solution. The solution is advanced up to $t = 0.5$, and it is shown in the right panel of Fig. 7.

In the left panel of Fig. 7, we have shown the solution of the same problem (on the same mesh and with the same CFL number) by the first-order upwind scheme on triangulations (see, e.g., [30,21] for an overview). We used the *local* Lax–Friedrichs (LLF), also known as Rusanov's, flux [35] for the upwind scheme because it provides good results, and it is easy to implement. In the case of a non-convex scalar equation such as (32) in conjunction with (33) and (34), the LLF flux is given by

$$\mathfrak{F}_{\mathrm{LLF}}(q_{\mathrm{L}}, q_{\mathrm{R}}) = \frac{1}{2}\big\{[u_{\mathrm{tot}}f(q_{\mathrm{L}})v_x + v_{\mathrm{tot}}g(q_{\mathrm{L}})v_y] + [u_{\mathrm{tot}}f(q_{\mathrm{R}})v_x + v_{\mathrm{tot}}g(q_{\mathrm{R}})v_y] - \alpha(q_{\mathrm{R}} - q_{\mathrm{L}})\big\}, \tag{36}$$
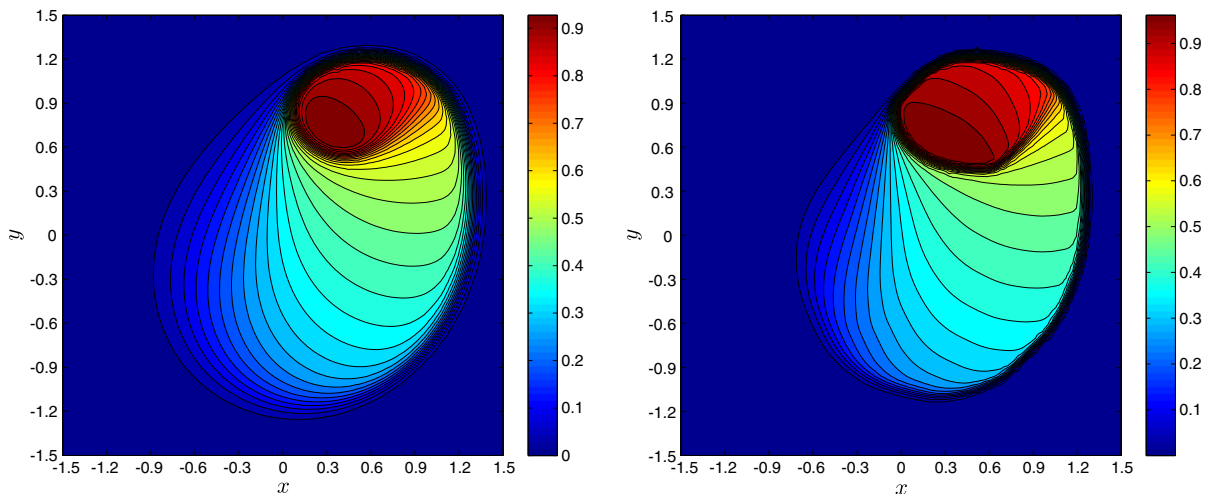

Fig. 7. Solutions to the Buckley–Leverett equation with gravity subject to the initial condition (35) by the first-order upwind scheme (left) and our JT-type second-order central scheme (right) at time $t = 0.5$ on a Friedrichs–Keller triangulation with $100 \times 100 \times 2$ elements; the CFL number is $C_{\mathrm{CFL}} = \frac{1}{3}$. Both the black and color contours are of the water saturation S_{w}.

where

$$\alpha := \max_{q \in [\min(q_L, q_R), \max(q_L, q_R)]} |u_{tot} f'(q) v_x + v_{tot} g'(q) v_y|, \tag{37}$$

$\boldsymbol{v} \equiv (v_x, v_y)^\top$ is a unit normal vector and q_L, q_R are the two states of the 1D Riemann problem to be solved in the direction of $\boldsymbol{v}$. Notice that given the variable nature of $\boldsymbol{v}$ and the particular form of the flux functions f and g, the computation of α requires finding the minimum of a different rational function along every different direction. Therefore, in practice, a reasonable upper bound is used for α, i.e., a quantity that is easy to compute but is still "local," e.g.,

$$
\begin{aligned}
\alpha &\leqslant |u_{tot} v_x| \max_{q \in [\min(q_L, q_R), \max(q_L, q_R)]} |f'(q)| + |v_{tot} v_y| \max_{q \in [\min(q_L, q_R), \max(q_L, q_R)]} |g'(q)| \\
&\leqslant (|u_{tot} v_x| + |v_{tot} v_y|) \max\{\max_{q \in [0,1]} |f'(q)|, \max_{q \in [0,1]} |g'(q)|\}.
\end{aligned}
\tag{38}
$$

This also illustrates the difficulty of implementing Godunov's flux (the least dissipative upwind flux [35]), which involves solving similar optimization problems to that of finding α, on unstructured triangulations, even for a scalar problem! The first-order upwind scheme does quite well, though there is some obvious smearing of ("leaking" from) the bottom of the rarefaction part of the composite wave and damping of the shock-wave part of the composite wave near the top of the plot (the upwind scheme predicts a smaller "eye" of the wave). Finally, we note that this is an "unfair" comparison since we are not comparing our second-order central to its first-order reduction, but that is precisely the point. Since the first-order upwind scheme is the workhorse of the oil industry [38,16], it is the goal of Fig. 7 to show that, especially when gravitational effects are present, our second-order central scheme performs much better on the same mesh, and it is far more flexible than the first-order upwind scheme(s).

3.5. Euler equations of gas dynamics

Moving on to hyperbolic *systems* of conservation laws, in this section, we discuss the solution of the celebrated Euler equations via the schemes we developed in Section 2. The latter are the governing equations for an ideal gas—i.e., the equations stating the conservation of mass, momentum and energy (see, e.g., [35] for an overview)—which in 2D take the form

$$
\partial_t \begin{pmatrix} \varrho \\ \varrho u \\ \varrho v \\ E \end{pmatrix} + \partial_x \begin{pmatrix} \varrho u \\ \varrho u^2 + p \\ \varrho u v \\ u(E + p) \end{pmatrix} + \partial_y \begin{pmatrix} \varrho v \\ \varrho u v \\ \varrho v^2 + p \\ v(E + p) \end{pmatrix} = 0, \tag{39}
$$

where ϱ is the density of the gas, p the pressure, u and v are the x- and y-velocities, respectively, and E is the total energy. The system is closed via the equation of state of an ideal gas:

$$p = (\gamma - 1) \left[E - \frac{\varrho}{2}(u^2 + v^2) \right], \tag{40}$$

where γ is the adiabatic index of the gas, i.e., the ratio of specific heats, which we take equal to 1.4 ($\Rightarrow$ the gas is air at 20 °C) for the purposes of this section. Below, we present numerical results for two standard test problems.

3.5.1. Four-state Riemann problem

For this problem, we divide the unit square $[0, 1]^2$ into four quadrants by the lines $x = \frac{1}{2}$ and $y = \frac{1}{2}$. Then, in each quadrant a different set of initial data is specified, possibly resulting in discontinuities along the quadrant boundaries. Also, it is common to specify the initial conditions for this Riemann problem in terms of the *primitive variables*, i.e., ϱ, u, v and p. Thus, we have that

$$
\begin{pmatrix} \varrho \\ u \\ v \\ p \end{pmatrix}(x,y,0) = \begin{cases} (\varrho_1, u_1, v_1, p_1)^\top, & x > 0.5, \ y > 0.5; \\ (\varrho_2, u_2, v_2, p_2)^\top, & x < 0.5, \ y > 0.5; \\ (\varrho_3, u_3, v_3, p_3)^\top, & x < 0.5, \ y < 0.5; \\ (\varrho_4, u_4, v_4, p_4)^\top, & x > 0.5, \ y < 0.5, \end{cases} \tag{41}
$$

where all the subscripted variables on the right-hand side are constants (see Table 8 for their values). We consider two specific cases (numbers 12 and 15) out of the 19 possible genuinely different configurations (see, e.g., [39] and the references therein for more details).

Unfortunately, the 2D Riemann problem is, in some sense, "artificial" in as much as there are no physical boundary conditions one can impose. Therefore, we were forced to solve the problem, which is posed on $[0, 1]^2$, on $\Omega = [-0.5, 1.5]^2$ using a set of stable (tough, perhaps, incorrect) boundary conditions on $\partial\Omega$. In this manner, for the Riemann problems considered in this section, any artificial boundary effects do no propagate into $[0, 1]^2$ and so we can display the results in the latter domain with confidence. (Note that this is not a problem when *physical* boundary conditions can be prescribed everywhere on $\partial\Omega$ as is the case in the next subsection.) In Fig. 8 we present plots of the solutions of the two representative Riemann problems by the JT-type scheme, which compare favorably with the results in [11,40,39].

Again (recall the mesh-size discussion in Section 3.2), in order to provide a fair comparison with the central-upwind schemes on structured triangulations in [11] and the various schemes on Cartesian tensor-product grids (including the original JT scheme) tested in [40], we compute the solution to (39) on a structured uniform Friedrichs–Keller triangulation with $400 \times 400 \times 2 \equiv 320,000$ elements (in $[0, 1]^2$). One can identify the latter

Table 8
The two sets of initial data that we consider for the four-state Riemann problem for the Euler equations

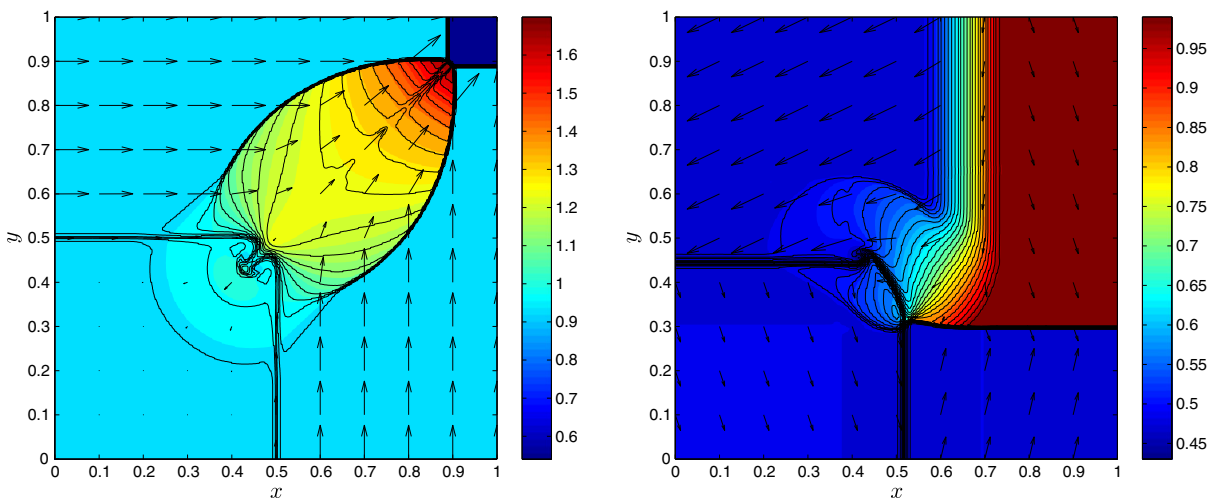| Case 12	Case 15
$(\varrho_1, u_1, v_1, p_1)^\top = (0.5313, 0.0, 0.0, 0.4)^\top$	$(\varrho_1, u_1, v_1, p_1)^\top = (1.0, 0.1, -0.3, 1.0)^\top$
$(\varrho_2, u_2, v_2, p_2)^\top = (1.0, 0.7276, 0.0, 1.0)^\top$	$(\varrho_2, u_2, v_2, p_2)^\top = (0.5197, -0.6259, -0.3, 0.4)^\top$
$(\varrho_3, u_3, v_3, p_3)^\top = (0.8, 0.0, 0.0, 1.0)^\top$	$(\varrho_3, u_3, v_3, p_3)^\top = (0.8, 0.1, -0.3, 0.4)^\top$
$(\varrho_4, u_4, v_4, p_4)^\top = (1.0, 0.0, 0.7276, 1.0)^\top$	$(\varrho_4, u_4, v_4, p_4)^\top = (0.5313, 0.1, 0.4276, 0.4)^\top$

Fig. 8. Plots of the solutions to (39) subject to (41), at $t = 0.25$ for case 12 (left) and at $t = 0.2$ for case 15 (right). The color/contour convention is that of [40]—i.e., the black contours are of the density ϱ (0.54–1.7 step 0.04 for case 12 and 0.43–0.99 step 0.02 for case 15), the color contours are of the pressure p (30 evenly spaced ones) and the arrows represent the velocity field $(u, v)^\top$. For both cases, the mesh is a Friedrichs–Keller triangulation with 320,000 elements (in $[0, 1]^2$), and the CFL number is $\frac{1}{3}$.

mesh with a 400×400 Cartesian tensor-product grid because both have the same (minimal) element edge length of $\frac{1}{400}$.

3.5.2. Mach 3 flow in a wind tunnel with a step

Next, we consider the now-common test problem proposed by Emery [41]—Mach 3 flow in a wind tunnel with a forward-facing step. The geometry of the domain is shown in the top panel of Fig. 9, and the initial conditions, which are (again) specified in terms of the primitive variables, are

$$(\rho, u, v, p)^\top(x, y, 0) = (1.4, 3.0, 0.0, 1.0)^\top. \tag{42}$$

Moreover, these initial conditions are prescribed as an inflow boundary condition along $x = 0$. Then, outflow boundary conditions are applied along $x = 3$. And, along the remaining parts of boundary, the solid wall or *slip* condition $uv_x + vv_y = 0$, where $(v_x, v_y)^\top$ is the outward unit normal to $\partial\Omega$, is enforced.

This problem was popularized by Woodward and Colella's extensive study [42], in which the piecewise-parabolic method (PPM) was used to generate benchmark solutions. The latter authors mention that the singular point at $(0.6, 0.2)$ must be treated with care in order to obtain a good quality solution. However, following [25], and because our scheme is built for unstructured triangulations, we simply refine the mesh near the singular point and do not do anything "special" there. The numerical solution is shown in the bottom panel of Fig. 9.

Our computational mesh, which is an unstructured non-uniform triangulation with 30,016 elements and 15,365 vertices (this corresponds to three uniform refinements of the mesh show in the top panel of Fig. 9), falls in-between the medium and fine meshes in [42] of "sizes" $\frac{1}{40}$ and $\frac{1}{80}$, respectively. So, our results are comparable to those in [23,25,28,42]. The reflected shock waves are a bit smeared (as is the case with the 3D central schemes discussed in [9]), but are clearly discernible, and the slip line above the Mach stem is not resolved on this mesh. However, the front shock is well-captured, so is the rarefaction near the singular point. Furthermore, we do not observe any noise or a boundary layer along the top of the step (see, e.g., [28,42]).
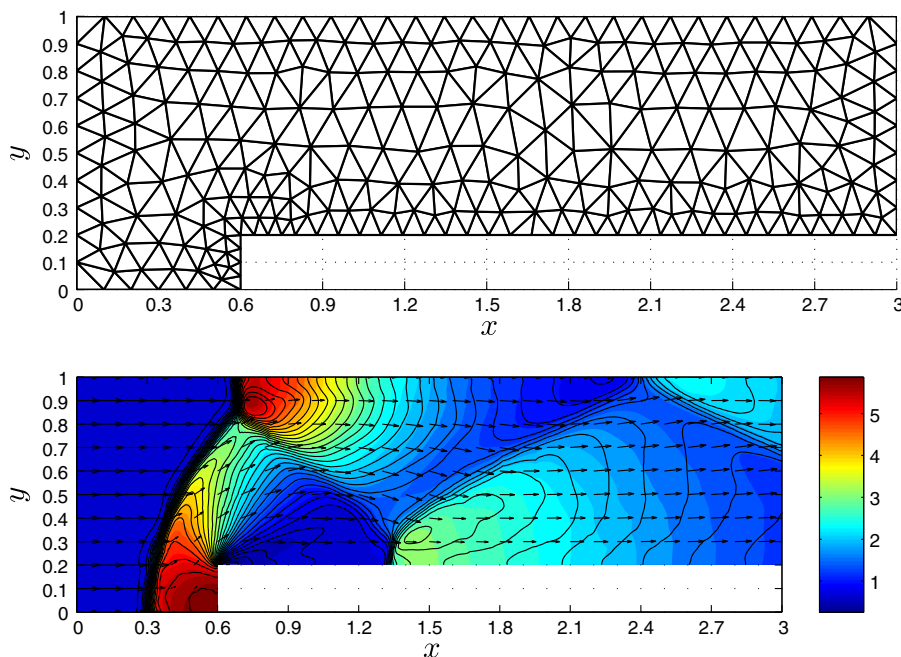

Fig. 9. The computational domain Ω with the coarsest mesh superimposed (top) and a plot of the solution to (39) subject to (42) at time $t = 4.0$ (bottom). The color/contour convention is that of [40]—i.e., the black contours are of the density ϱ (0.2568–6.067 step 0.1937), the color contours are of the pressure p (30 evenly spaced ones) and the arrows represent the velocity field $(u, v)^\top$. The mesh is an unstructured non-uniform triangulation with 30,016 elements (i.e., the mesh shown in the top panel uniformly refined three times), and the CFL number is $\frac{1}{9}$.

4. Conclusions and future work

In this paper, we introduced a new family of fully-discrete high-order central Godunov-type schemes on unstructured triangulations. Along the way, we proposed a novel non-oscillatory reconstruction, the MAPR, based on the adaptive selection of the "flattest" interpolating plane. The MAPR is simple, effective and easy to implement on the staggered mesh as well as on the original triangulation. In this respect, our scheme is an improvement over the one presented in [4], where a different reconstruction and limiting procedure is used on each mesh, resulting in a very restrictive CFL condition. Moreover, because our scheme is fully-discrete, it is easier to implement on truly unstructured meshes than the *semi*-discrete scheme proposed in [11]. This makes the present numerical method *very* flexible and extensible, which is important for IMPES algorithms used in reservoir flow simulations (see Section 3.4). In this respect, even though we only discussed the case of an unstructured triangulation as the original mesh, the extension of the central schemes discussed in this paper to more elaborate unstructured meshes and geometries (such as the *corner-point geometry* or *perpendicular bisector* grids commonly used in the oil industry [43]) is straightforward, since the scheme can be implemented with "off-the-shelf" tools (i.e., standard mesh data structures, interpolation/projection operators, etc.). Furthermore, the extension to 3D (unstructured tetrahedral meshes) can be done along the same lines as earlier extensions of 1D and 2D central schemes to 3D (see, e.g., the work of Arminjon et al. [9,10] and the references therein). The MAPR immediately generalizes to any number of dimensions using the concept of a *hyperplane*. However, in dimensions greater than two, building the staggered mesh for the KT-type scheme at each time step may be prohibitively expensive. In this case, one can may have to use the JT-type scheme, since the mesh for the latter only needs to be constructed once.

At this point, we would like to mention that local adaptive mesh refinement (AMR) can be incorporated seamlessly into our algorithm. For example, one could use a simple refinement indicator, such as those proposed in [30, pp. 258–275], to refine and coarsen the mesh at each time step, depending on where the discontinuities in the solution propagate. In this respect, unstructured triangulations are the easiest to handle because local refinement does not introduce non-conforming nodes, which require extra care to be taken to enforce conservation there (see [44]). As far as central schemes are concerned, an AMR algorithm for the case of a 2D triangular mesh and a staggered mesh consisting of centroid-median cells (similar to the Voronoi diagram special case of our staggerd mesh, see [31, pp. 35–39]) was proposed in [36] and shows promise. In addition, Noelle et al.'s recent work [45] shows that a central scheme with AMR can be implemented on non-matching (i.e., non-conforming) Cartesian grids in 3D extending the "classical" hydrodynamics AMR framework [44]. Also, within the AMR framework of [44], a theoretically-motivated smoothness indicator for conservation laws based on the so-called weak *Lip*'-norm, which can be used as a refinement indicator, was developed in [46]. Another approach to adaptivity could be to use a moving-mesh method such as that of Tang and Tang [47] to align the mesh with the important features of the flow.

Finally, we believe that it is possible to prove that, at least in the case of the JT-type scheme (i.e., when the staggered mesh does not change in time), the central scheme using the minimum-angle plane reconstruction satisfies a maximum principle. Results in this direction will be presented in future work. Other avenues of further work are the evaluation of the MAPR's performance in upwind schemes and the study of "incomplete" reconstructions, i.e., when only a certain well-chosen set of interpolating planes are considered instead of the all the possible ones.

References

[1] H. Nessyahu, E. Tadmor, Non-oscillatory central differencing for hyperbolic conservation laws, J. Comput. Phys. 87 (1990) 408–463.

[2] B. van Leer, Towards the ultimate conservative difference scheme. V. A second-order sequel to Godunov's method, J. Comput. Phys. 32 (1979) 101–136.

[3] B. Popov, O. Trifonov, One-sided stability and convergence of the Nessyahu–Tadmor scheme, Numer. Math. 104 (2006) 539–559.

[4] P. Arminjon, M.-C. Viallon, A. Madrane, A finite volume extension of the Lax–Friedrichs and Nessyahu–Tadmor schemes for conservation laws on unstructured grids, Int. J. Comput. Fluid Dyn. 9 (1997) 1–22.

[5] G.-S. Jiang, E. Tadmor, Nonoscillatory central schemes for multidimensional hyperbolic conservation laws, SIAM J. Sci. Comput. 19 (1998) 1892–1917.

[6] G.-S. Jiang, D. Levy, C.-T. Lin, S. Osher, E. Tadmor, High-resolution nonoscillatory central schemes with nonstaggered grids for hyperbolic conservation laws, SIAM J. Numer. Anal. 35 (1998) 2147–2168.

[7] A. Kurganov, E. Tadmor, New high-resolution central schemes for nonlinear conservation laws and convection–diffusion equations, J. Comput. Phys. 160 (2000) 241–282.

[8] A. Kurganov, S. Noelle, G. Petrova, Semidiscrete central-upwind schemes for hyperbolic conservation laws and Hamilton–Jacobi equations, SIAM J. Sci. Comput. 23 (2001) 707–740.

[9] P. Arminjon, A. St-Cyr, A. Madrane, New two- and three-dimensional non-oscillatory central finite volume methods on staggered Cartesian grids, Appl. Numer. Math. 40 (2002) 367–390.

[10] P. Arminjon, A. St-Cyr, Nessyahu–Tadmor-type central finite volume methods without predictor for 3D Cartesian and unstructured tetrahedral grids, Appl. Numer. Math. 46 (2003) 135–155.

[11] A. Kurganov, G. Petrova, Central-upwind schemes on triangular grids for hyperbolic systems of conservation laws, Numer. Methods Partial Differential Eq. 21 (2005) 536–552.

[12] A. Kurganov, G. Petrova, B. Popov, Adaptive semi-discrete central-upwind schemes for nonconvex hyperbolic conservation laws, SIAM J. Sci. Comput. 29 (2007) 2381–2401.

[13] I. Christov, B. Popov, A Jiang–Tadmor scheme on unstructured triangulations, Technical Report ISC-06-05-MATH, Institute for Scientific Computation, Texas A&M University, College Station, TX, 2006.

[14] J.-L. Guermond, A finite element technique for solving first-order PDEs in L^p, SIAM J. Numer. Anal. 42 (2004) 714–737.

[15] J.-L. Guermond, B. Popov, Linear advection with ill-posed boundary conditions via L^1-minimization, Int. J. Numer. Anal. Mod. 4 (2007) 39–47.

[16] M.G. Gerritsen, L.J. Durlofsky, Modeling fluid flow in oil reservoirs, Annu. Rev. Fluid Mech. 37 (2005) 211–238.

[17] M. Käser, A. Iske, Reservoir flow simulation by adaptive ADER schemes, in: A. Iske, T. Randen (Eds.), Mathematical Methods and Modelling in Hydrocarbon Exploration and Production, Mathematics in Industry, vol. 7, Springer, Berlin/Heidelberg, 2005, pp. 339–388.

[18] P. Knabner, L. Angermann, Numerical Methods for Elliptic and Parabolic Partial Differential Equations, Texts in Applied Mathematics, vol. 44, Springer, Berlin/Heidelberg, 2003.

[19] L.J. Durlofsky, B. Engquist, S. Osher, Triangle based adaptive stencils for the solution of hyperbolic conservation laws, J. Comput. Phys. 98 (1992) 64–73.

[20] P. Batten, C. Lambert, D.M. Causon, Positively conservative high-resolution convection schemes for unstructured elements, Int. J. Numer. Methods Eng. 39 (1996) 1821–1838.

[21] M.E. Hubbard, Multidimensional slope limiters for MUSCL-type finite volume schemes on unstructured grids, J. Comput. Phys. 155 (1999) 54–74.

[22] M. Wierse, A new theoretically motivated higher order upwind scheme on unstructured grids of simplices, Adv. Comput. Math. 7 (1997) 303–335.

[23] R. Abgrall, On essentially non-oscillatory schemes on unstructured meshes: analysis and implementation, J. Comput. Phys. 114 (1994) 45–58.

[24] O. Friedrich, Weighted essentially non-oscillatory schemes for the interpolation of mean values on unstructured grids, J. Comput. Phys. 144 (1998) 194–212.

[25] C. Hu, C.-W. Shu, Weighted essentially non-oscillatory schemes on triangular meshes, J. Comput. Phys. 150 (1999) 97–127.

[26] H.J. Schroll, F. Svensson, A bi-hyperbolic finite volume method on quadrilateral meshes, J. Sci. Comput. 26 (2006) 237–260.

[27] R. Artebrant, Third order accurate non-polynomial reconstruction on rectangular and triangular meshes, J. Sci. Comput. 30 (2007) 193–221.

[28] C. Berthon, Robustness of MUSCL schemes for 2D unstructured meshes, J. Comput. Phys. 218 (2006) 495–509.

[29] B. Perthame, Y. Qiu, A variant of Van Leer's method for multidimensional systems of conservation laws, J. Comput. Phys. 112 (1994) 370–381.

[30] D. Kröner, Numerical Schemes for Conservation Laws, Wiley–Teubner, Chichester, NY, 1997.

[31] T. Barth, M. Ohlberger, Finite volume methods: foundation and analysis, in: E. Stein, R. de Borst, T.J.R. Hughes (Eds.), Encyclopedia of Computational Mechanics, Wiley, 2004, pp. 1–57.

[32] A. Harten, S. Osher, Uniformly high-order accurate nonoscillatory schemes. I, SIAM J. Numer. Anal. 24 (1987) 279–309.

[33] M. Käser, A. Iske, ADER schemes on adaptive triangular meshes for scalar conservation laws, J. Comput. Phys. 205 (2005) 486–508.

[34] K.-A. Lie, S. Noelle, An improved quadrature rule for the flux-computation in staggered central difference schemes in multidimensions, J. Sci. Comput. 18 (2003) 69–81.

[35] R.J. LeVeque, Finite-Volume Methods for Hyperbolic Problems, Cambridge Texts in Applied Mathematics, vol. 31, Cambridge University Press, 2002.

[36] M. Küther, M. Ohlberger, Adaptive second order central schemes on unstructured staggered grids, in: T.Y. Hou, E. Tadmor (Eds.), Hyperbolic Problems: Theory, Numerics, Applications, Springer, Berlin/Heidelberg, 2003, pp. 675–684.

[37] E.F. Kaasschieter, Solving the Buckley–Leverett equation with gravity in a heterogeneous porous medium, Comput. Geosci. 3 (1999) 23–48.

[38] J.E. Aarnes, T. Gimse, K.-A. Lie, An introduction to the numerics of flow in porous media using Matlab, in: G. Hasle, K.-A. Lie, E. Quak (Eds.), Geometric Modelling, Numerical Simulation, and Optimization: Applied Mathematics at SINTEF, Springer, Berlin/Heidelberg, 2007, pp. 261–302.

[39] A. Kurganov, E. Tadmor, Solution of two-dimensional Riemann problems for gas dynamics without Riemann problem solvers, Numer. Methods Partial Differential Eq. 18 (2002) 584–608.

[40] R. Liska, B. Wendroff, Comparison of several difference schemes on 1D and 2D test problems for the euler equations, SIAM J. Sci. Comput. 25 (2003) 995–1017, <http://www-troja.fjfi.cvut.cz/liska/CompareEuler/compare8/>.

[41] A.F. Emery, An evaluation of several differencing methods for inviscid fluid flow problems, J. Comput. Phys. 2 (1968) 306–331.

[42] P. Woodward, P. Colella, The numerical simulation of two-dimensional fluid flow with strong shocks, J. Comput. Phys. 54 (1984) 115–173.

[43] G. Adamson, M. Crick, B. Gane, O. Gurpinar, J. Hardiman, D. Ponting, Simulation throughout the life of a reservoir, Oilfield Rev. 8 (1996) 16–27.

[44] M.J. Berger, P. Colella, Local adaptive mesh refinement for shock hydrodynamics, J. Comput. Phys. 82 (1989) 64–84.

[45] S. Noelle, W. Rosenbaum, M. Rumpf, 3D adaptive central schemes: Part I. Algorithms for assembling the dual mesh, Appl. Numer. Math. 56 (2006) 778–799.

[46] S. Karni, A. Kurganov, G. Petrova, A smoothness indicator for adaptive algorithms for hyperbolic systems, J. Comput. Phys. 178 (2002) 323–341.

[47] H. Tang, T. Tang, Adaptive mesh methods for one- and two-dimensional hyperbolic conservation laws, SIAM J. Numer. Anal. 41 (2003) 487–515.